

Enhanced iron impurity removal in low iron Al-Si alloys by Mn addition

ABDULLAH HARAZEEN*, LUCIA LATTANZI, TAISHI MATSUSHITA AND
ANDERS E. W. JARFORS

*Department of Materials and Manufacturing, School of Engineering,
Jönköping University, Gjuterigatan 5, SE-551 11 Jönköping, Sweden*

Received: July 16, 2024; Accepted: October 23, 2024.

Over the past decades, demand for high-purity aluminium (Al) has increased in many sectors, like aerospace and automotive sectors, since it combines a high level of purity with the flexibility of controlled alloying, which allows for tailored enhancements of material properties. To accommodate the rising demand, primary Al production has significantly increased since the refining of secondary Al is constrained by high impurity levels, especially iron (Fe). A way to mitigate this problem is to add Fe-bearing intermetallic particle formers, like manganese (Mn). This paper investigates the influence of different Mn additions for low-Fe composition aluminium melts at a cooling rate of 3 °C/min, as the primary Fe-rich phases may differ and cannot be extrapolated. More specifically, the impact of filters, the Fe removal efficiency for different Mn additions, and the Fe-bearing intermetallic particles' Fe removal potential. Fe removal potential was evaluated by combining intermetallic particle area fraction with their average Fe content. This was done by running Thermo-Calc equilibrium calculations to guide the planning of the experimental work. Then, running small-scale experiments with 8 kg of Al-11Si-0.5Fe alloy. The study concludes that the Fe-bearing intermetallic particles sedimented at the bottom of the furnace since the composition of the filtered and unfiltered samples from the top part of the melt was similar. Additionally, larger amounts of Mn are required to improve the Fe removal efficiency for low-Fe concentration Al-Si cast alloys since it improves the Fe removal potential and increases the amount of Fe-bearing intermetallic particles in the melt.

Keywords: Al-Si alloy, Purification, Sludge, Fe-bearing intermetallic particles, Manganese, Scanning electron microscopy, Fe removal, Refining, Cleaning, Microstructure

*Corresponding author: Abdullah.harazeen@ju.se

1 INTRODUCTION

The demand for aluminium (Al) has significantly increased over the past decades for the automotive and aerospace industries since it combines a high level of purity with the flexibility of controlled alloying, which allows for tailored enhancements of material properties. Additionally, it has many favourable characteristics like a high strength-to-weight ratio, high electric and thermal conductivity and low density [1, 2]. More primary aluminium is produced to cope with this demand, which is problematic since every kg of primary aluminium will typically generate 12 kg of CO₂ [3]. Recycling aluminium scrap is one of the best ways to follow a circular economy because aluminium can be recycled without degrading its properties and helps close the production loop [4]. In addition, aluminium recycling emits approximately 0.6 kg of CO₂ for every kg produced, considerably lower than the emissions from primary aluminium production [5].

However, refining secondary aluminium is necessary to remove impurities like tramp elements, undesired alloying elements and inclusions from the melt. These impurities can cause various problems, including increased porosities, decreased melt fluidity, poor machinability, and negatively affecting the material's mechanical properties [6]. As a result, refining and controlling these impurities is a challenge. This challenge will significantly intensify in the coming years, mainly in the recycling process of aluminium, since the demand for high-quality Al will increase (to reduce carbon emission), which will lead to a decrease in the availability of high-quality scrap, and an increase in the availability of low-quality contaminated scrap [3].

Iron (Fe) impurity is a significant problem for secondary aluminium due to its detrimental effects on mechanical and casting properties [7]. The alloy addition method is most effective for Fe-containing Al-Si cast alloys. However, this will not be a problem since, according to Sanchez *et al.* [8] and Hegde *et al.* [9], approximately 80% of the employed aluminium casting alloys in the manufacturing industry are Al-Si alloys. The most harmful phase in this alloy is the β -Al₅SiFe phase from its brittleness and morphology, affecting its mechanical properties. Additionally, the structure of the β -Al₅SiFe appears to be like a coarse plate with sharp edges that increase the stress concentration, reducing the aluminium alloy's ductility and fluidity of the melt [7]. Therefore, Fe reduction in the melt is crucial to mitigate this problem.

One way to reduce Fe from the aluminium melt is by adding elements referred to as sludge formers in the literature [10]. In this paper, the term "sludge" was clarified to refer specifically to Fe-bearing intermetallic particles, as "sludge" is a broad term that could lead to a misunderstanding. This method promotes the formation of Fe-bearing intermetallic particles, which could be later removed by either filtration or sedimentation. Some transition

metals like nickel (Ni), manganese (Mn), chromium (Cr), cobalt (Co), vanadium (V) and titanium (Ti) alloys are the Fe-bearing intermetallic particle formers that could be used to decrease the Fe content in the melt [11].

Some research papers have tested different transition elements, and the most used elements to reduce the Fe content in the melt are Cr and Mn. Dietrich et al. [7] showed that, for Al-9Si-3Cu(Fe) alloys, Mn generates larger Fe-bearing intermetallic particles with higher particle density. As a result, particles sink to the bottom of the melt easily (easily removed by either decanting or filtration). Cr generates greater numbers of smaller Fe-bearing intermetallic particles with lower density, making them harder to remove [7]. To mitigate this problem, a combination of Mn and Cr alloys provides efficient and effective Fe-bearing intermetallic particle creation and, in turn, decreases the Fe content in the melt [7]. It is crucial to remember that although Mn and Cr convert the harmful β -Al₅SiFe intermetallic phase to a more harmless intermetallic phase and morphology, it also creates more intermetallic particles that need removal.

Many research studies have shown that adding different amounts of Fe-bearing intermetallic particle formers to high-Fe aluminium alloys improves the Fe removal efficiency [7, 12, 13]. For example, Ferraro et al. [12] showed that for Al-9Si-3Cu(Fe) alloy, varying levels of Fe, Mn, and Cr affect the Fe-bearing intermetallic particle formation, size and density. In another study, Song et al. [13] also investigated the effectiveness of the Mn/Fe ratio on Fe removal from an Al-7.0Si-2.4Fe alloy and how varying initial Fe content affects the microstructure and mechanical properties of the alloy. Also, as the Mn/Fe ratio increases, the type of primary Fe-rich phase gradually changes from α -Al₈Fe₂Si to α -Al₁₅(FeMn)₃Si₂ [13].

Published research papers on the Fe refining method investigated the use of melts with high initial Fe content (0.8-2 wt%). These results show that the Fe-bearing intermetallic formation method's efficiency in reducing the Fe content and particle population was not investigated for low initial Fe content in the melt. These data cannot be extrapolated since the primary Fe-rich phase may differ. This paper investigates the influence of different Mn additions on the Fe removal efficiency for low Fe composition aluminium melts at a constant cooling rate. In addition to that, the impact of using filters was tested. The characteristics of the Fe-bearing intermetallic particles were quantified using image analysis and energy dispersive x-ray spectroscopy to find the Fe-removal potential of different Mn additions.

2 MATERIALS AND EXPERIMENTAL METHODOLOGY

2.1 Materials

This study used a secondary aluminium Al-Si alloy (EN AB-44300 aluminium alloy, Stena Aluminium AB, Sweden) with 0.5 wt% Fe, as a base alloy.

The chemical composition of the EN AB-44300, obtained using optical emission spectroscopy SPECTROMAXx CCD LMXM3 (AMETEK), is shown in Table 1.

2.2 Sample preparation and production

Small-scale experiments were conducted in which 8 kg of aluminium was melted per experiment in a tilting furnace. Two different alloys were prepared using varying Mn compositions based on thermodynamic phase diagram calculations using Thermo-Calc. The master alloy used to obtain the desired compositions was a Al-80Mn type alloy.

The melt was heated up to 1073 K. Then, it cooled at 3 K/min. In the cooling stage, the sampling was made at different temperatures. Two to three samples were taken before the Fe-bearing intermetallic particle formation temperature. Then, two to five samples were taken after the calculated Fe-bearing intermetallic particle formation temperature, depending on the difference between the Fe-bearing intermetallic particle formation temperature and the FCC formation temperature. The Fe-bearing intermetallic particles formation temperature was obtained from Thermo-Calc Software TCAL8/Al-alloys Database version 8.2 [14]. A total of seven samples were taken from the top of the crucible. The samples were taken from the top of the melt to assess the Fe cleaning efficiency at different temperatures since the Fe-bearing intermetallic particles are expected to sediment. In the end, a sample from the bottom of the crucible was taken to analyse the remaining residue.

The samples were taken from the top of the crucible (20 cm diameter \times 25 cm height) using a scoop and poured into a 3 cm diameter and 1.5 cm coin-shaped mould. A trough-type fibreglass mesh filter (Pyrotek) with a hole size of 0.0138 cm² was also fixed on top of the mould.

TABLE 1
Chemical composition (wt%) and the standard deviation (STD) of EN AB-44300 aluminium alloy and the experimental alloys.

Alloy Name		Si	Fe	Mn	Cr	Cu	Mg	Ni	Ti	Al
EN AB 44300	Comp (wt%)	11.0	0.51	0.11	0.01	0.06	0.02	0.01	0.04	Bal
	STD	0.2	0.01	<0.01	<0.01	<0.01	<0.01	<0.01	<0.01	–
0.6Mn	Comp (wt%)	11.0	0.46	0.58	0.01	0.06	0.01	0.01	0.04	Bal
	STD	0.02	<0.01	<0.01	<0.01	<0.01	<0.01	<0.01	<0.01	–
1.5Mn	Comp (wt%)	10.8	0.51	1.59	0.01	0.06	0.005	0.01	0.04	Bal
	STD	0.1	0.04	0.17	<0.01	<0.01	<0.01	<0.01	<0.01	–

2.3 Material characterisation

Metallographic preparations were performed on the samples. These preparations comprise cutting and grinding of the samples to get a smooth flat surface. After that, the sample's chemical composition was identified using the spectrometer. A total of four points were analysed per sample. Regarding the sample taken from the bottom of the crucible, it was grinded and polished for metallographic observations and to characterise the intermetallic particles' with chemical composition and population size using scanning electron microscopy (SEM, Tescan LYRA3) and energy-dispersive X-ray spectroscopy (EDS, Edax Octane Plus). The backscattered electrons detector in the SEM was used to perform quantitative image analysis and describe the geometrical features of the particles' population. The Fe-bearing intermetallic particles were identified by analysing the composition of different particles using EDS. The particles with Mn, Fe and Si in their composition are the Fe-bearing intermetallic particles.

The population of the Fe-based particles at the bottom of the crucible sample was quantitatively analysed on a $1018\ \mu\text{m} \times 2036\ \mu\text{m}$ region using MIPAR as the image analysis software. A total of 18 (3 x 6) images with a field of view of $340\ \mu\text{m}$ at a random position on the sample were first taken using Olympus DSX1000 optical microscope. Then, the images were imported to the MIPAR software, and the Fe-bearing intermetallic particles, identified using EDS, were selected. After that, the MIPAR software was run to determine the Fe-bearing intermetallic particle amount, calliper diameter and area.

3 RESULTS AND DISCUSSION

3.1 Mn composition addition selection

To decide the amount of Mn to add, a thermodynamic calculation was made using Thermo-Calc. The stable phase(s) at each temperature and Mn amount were calculated as shown in the phase diagram (Figure 1). Based on the calculations, two Mn concentrations were chosen: 0.6 wt% Mn, where the Fe-bearing intermetallic particles start to be the primary precipitating phase at 873 K, and 1.5 wt% Mn, where the Fe-bearing intermetallic particle formation temperature is relatively high (923 K).

3.2 Calculated Fe-bearing intermetallic particles' formation starting point

Equilibrium calculations were performed in Thermo-Calc to estimate the Fe-bearing intermetallic particle formation temperature. The volume fraction of phases against temperature was calculated for the given alloy composition. The results are shown in Figures 2a and 2b. In this case, the Fe-bearing intermetallic particle phase is $\text{Al}_{15}\text{Si}_2\text{M}_4$, where M is (Cr, Fe, Mn, Mo). These figures show that the Fe-bearing intermetallic particle formation points start

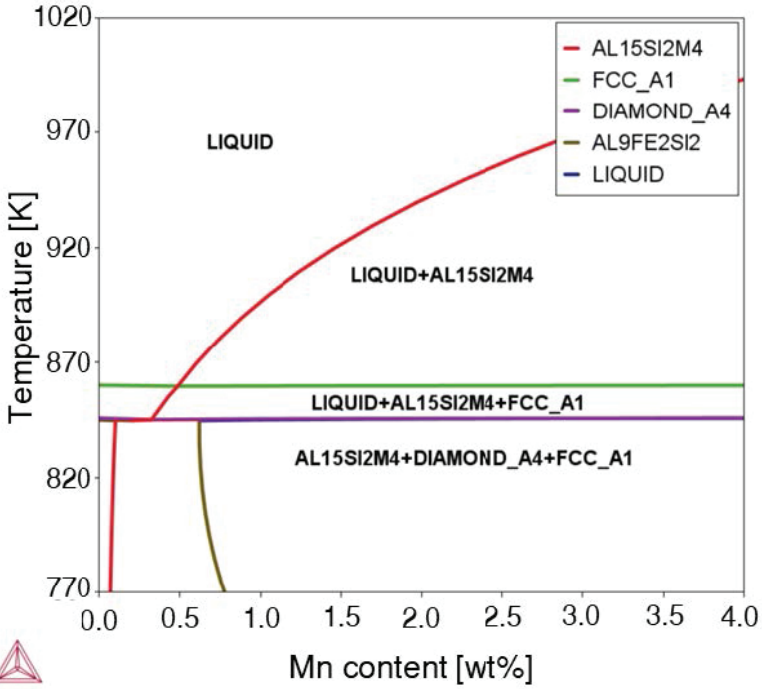


FIGURE 1
The vertical section of the phase diagram shows the effect of Mn-composition on an EN AB-44300 aluminium alloy.

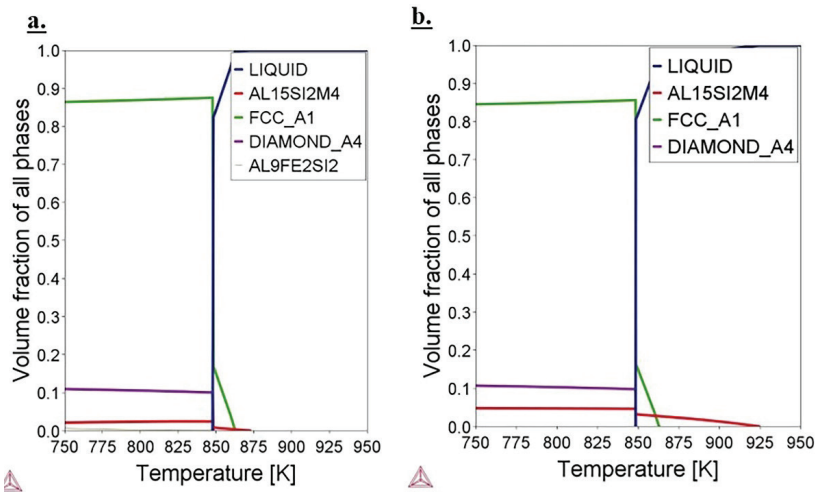


FIGURE 2
Thermo-Calc calculation for the phase volume fractions for the a) 0.6Mn alloy and b) 1.5Mn alloy.

for 0.6Mn and 1.5Mn at 873 and 926 K, respectively. Also, the volume fraction of the $Al_{15}Si_2M_4$ phase at higher temperatures is low in the 0.6Mn (0.022) alloy compared to the 1.5Mn (0.048) alloy. The differences in the formation temperature and volume fraction of the Fe-bearing particles highlight the influence of the Mn addition on the Fe-bearing intermetallic particles and their amount. In addition, the phase diagram (Figure 1) and the equilibrium calculation graph (Figure 2) show that adding Mn to the alloy promotes the formation of the Fe-bearing intermetallic particles.

3.3 Effect of Mn addition on Fe-bearing intermetallic particles' formation

Two different alloys with different Mn compositions were prepared for this study. Table 2 shows the Fe-bearing intermetallic particle formation temperatures using Thermo-Calc software. Then, the experiment was performed.

After the experiment was performed and the samples were taken, the sample's element composition was identified using the spectrometer to obtain Fe and Mn content in the melt at different temperatures. The results of both the filtered and the unfiltered data are summarised in Figures 3a and 3b.

Figures 3a and 3b show that the average contents of Fe and Mn of the filtered and unfiltered samples for both alloys were reasonably similar when considering the standard deviation since the content variation between the filtered and unfiltered samples were similar. One reason for the Fe and Mn content similarity between the filtered and unfiltered samples was the sampling method; both samples were taken from the top of the melt. This indicates that few large Fe-bearing intermetallic particles were present at the top of the melt that could be filtered out.

Then, the Fe and Mn removal composition reduction percentage was calculated using Equation 1.

$$CR = \frac{C_{\text{initial}} - C_{\text{final}}}{C_{\text{initial}}} \times 100 \quad (1)$$

where CR is composition reduction (%), C_{initial} is the initial composition of the melt before starting the experiment (wt%), and C_{final} is the final composition at the lowest temperature (wt%). When adding 0.6Mn, the Fe and Mn content of the samples decreases by 31 % and 38 %, respectively. The main decrease

TABLE 2

Experimental alloys targeted and achieved (in parenthesis) initial compositions of Fe and Mn composition.

Alloy Name	Calculated Fe-Bearing Intermetallic Formation Temperature (°C)	Calculated FCC Formation Temperature (°C)
0.6Mn	600	590
1.5Mn	653	590

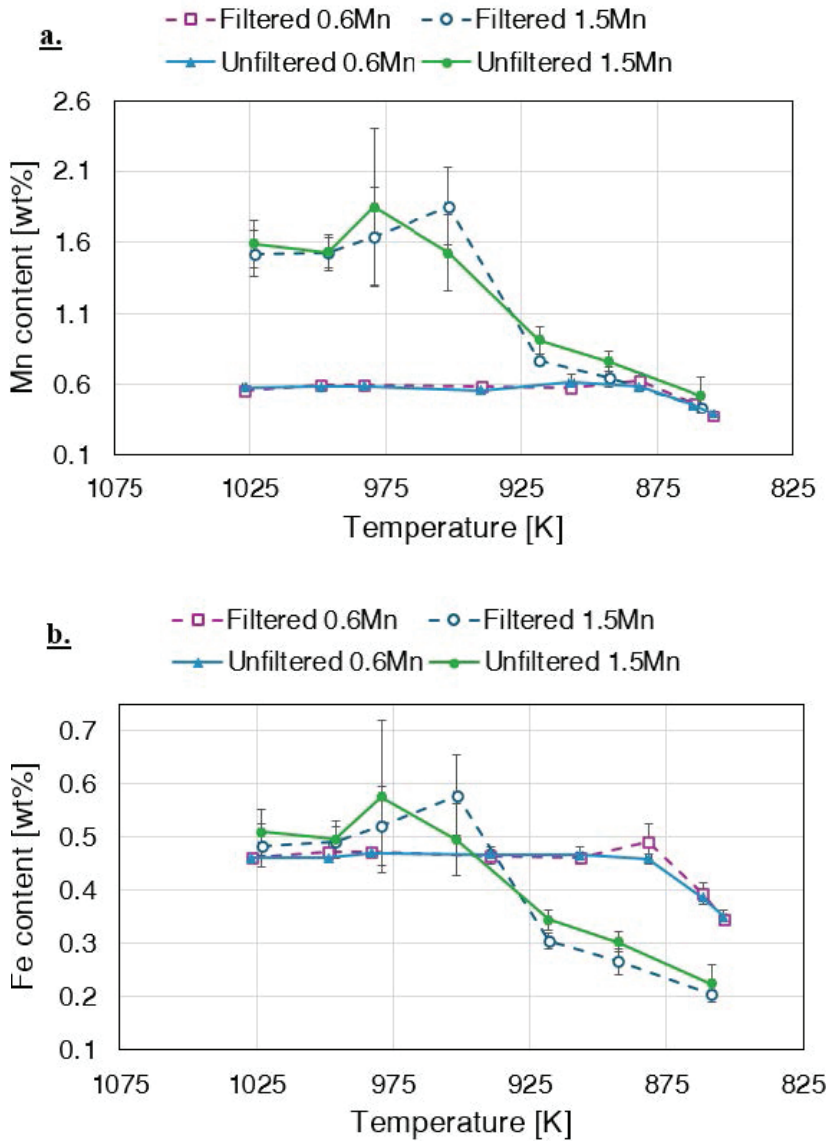


FIGURE 3

Experimentally obtained compositions, at the top of the melt, as a function of temperature for the 0.6Mn and 1.5Mn in the filtered and unfiltered conditions with a) Mn composition and b) Fe composition.

occurred when the melt temperature was at around 883 K. For the 1.5Mn addition, the Fe and Mn content of the samples decreased by 59 % and 71 %, respectively. The Fe and Mn content reduction was almost twice that observed with a 0.6Mn addition. Both Fe and Mn content started to decrease at a temperature of 979 K.

The results show that using Fe-bearing intermetallic particle formers, Mn in this case, works for lower Fe compositions in the melt. However, larger amounts of Mn are required to decrease efficiently the Fe content in the melt.

3.4 Fe-bearing intermetallic particles analysis

In order to characterise the Fe-bearing intermetallic particles, a sample was taken from the bottom of the crucible. After that, SEM and MIPAR tools were used to analyse the microstructure and chemical composition of the Fe-bearing intermetallic particles.

The particle analysis was performed on the sample on a $1018 \times 2036 \mu\text{m}$ area from the residual sample's bottom plane. The Fe-bearing intermetallic particle area fraction and the number of particles for 0.6Mn and 1.5Mn samples are summarised in Table 3. The table shows that the cross-section area of the Fe-bearing intermetallic particle when adding 1.5 Mn was almost three times that of 0.6 Mn addition. It has been reported by Dietrich et al. [7] and Ferraro et al. [12] that the higher the Mn/Fe ratio, the higher the area fraction of the Fe-bearing intermetallic particles for alloys with higher initial Fe content in the melt. Similar results are observed for the performed experiments in this paper for lower initial Fe content. However, the area fraction of the Fe-bearing intermetallic particles is lower for lower initial Fe content.

The volume fraction of Fe-bearing intermetallic particles obtained from Thermo-Calc (Figure 2) are comparable with the experimental area fraction (Table 3). The comparable values are because the experimental area fraction represents an average area fraction from multiple observation planes, assuming a uniform and isotropic microstructure. Therefore, the experimental area fraction from different random sections approximates the volume fraction.

TABLE 3
Fe-bearing intermetallic particles analysis at the lowest temperature and bottom of crucible samples

Alloy Name	Fe-bearing intermetallic particles area fraction (%)		Total number of Fe-bearing intermetallic particles	
	Bottom of crucible	Top of crucible at the lowest temperature	Bottom of crucible	Top of crucible at the lowest temperature
0.6Mn	1.9 ± 0.5	0.3 ± 0.5	88	31
1.5Mn	5.3 ± 0.9	0.7 ± 1.1	273	42

According to the Thermo-Calc calculation shown in Figure 2, the volume fractions of 0.6Mn and 1.5Mn alloys are 2.4 and 5.7 %, respectively, while the area fractions of both experiments are summarised in Table 3. When comparing these data, the Thermo-Calc estimation of the volume fraction of Fe-bearing intermetallic particles generated after the solidification of the alloy aligns with the experimental results for 0.6Mn and 1.5Mn alloys. The Thermo-Calc calculated volume fraction is within the standard deviation of the experimental area fraction of the Fe-bearing intermetallic particles.

A histogram plot of the probability density function (PDF) against the Feret diameter of the Fe-bearing particle, where the Feret diameter is a measure of the longest distance across the particle, was plotted in Figure 4a. The PDF is a function used to describe the likelihood of a continuous random variable taking a particular value. It helps provide a complete description of the distribution of the Feret diameter to describe the Fe-bearing intermetallic particles. Figure 4a illustrates the impact of Mn addition on the size distribution of the Fe-bearing intermetallic particles. The 0.6Mn addition results in larger amounts of small Feret diameter Fe-bearing particles than the 1.5Mn addition. However, the largest particle had a Feret diameter of 80 μm , while 1.5Mn addition generated larger particles that go up to 120 μm . In addition to that, the 1.5Mn alloy precipitated a greater number of Fe-bearing intermetallic particles than the 0.6 Mn addition.

Given that the particle diameter data was left-skewed in Figure 4a, the particle size histogram was fitted with a lognormal distribution (Figure 4b). The lognormal distribution was chosen since it allows for a more accurate representation of the particle size distribution compared to the normal distribution, providing a robust framework for subsequent statistical analysis and interpretation. Figure 4b demonstrates the efficacy of the lognormal model in capturing the asymmetry and spread of the particle's Feret diameter. The peak of the PDF indicates the mode (data most concentrated) of the Fe-bearing intermetallic particle distribution. The curve's width demonstrates the variance (spread) of the data. While the tail of the curve represents the likelihood of having extreme values. When comparing 0.6Mn and 1.5Mn addition, Figure 4b shows that the peak of the 0.6Mn was higher than 1.5Mn addition, which means a higher frequency of small particles. While the tail of the curve for 0.6 and 1.5Mn alloys were almost the same.

These findings suggest that higher Mn concentrations promote the formation and growth of the Fe-bearing intermetallic particles both in terms of size and quantity. The increase in the number and size of the Fe-bearing intermetallic particles with higher Mn addition could be attributed to enhanced nucleation, particle coalescence, and growth kinetics facilitated by the increase in the Mn content. This behaviour emphasises the crucial role of the alloying elements in controlling the microstructure and, consequently, the material's properties. Future work needs to be done focusing on optimising Mn concentrations to achieve a desirable balance between particle size

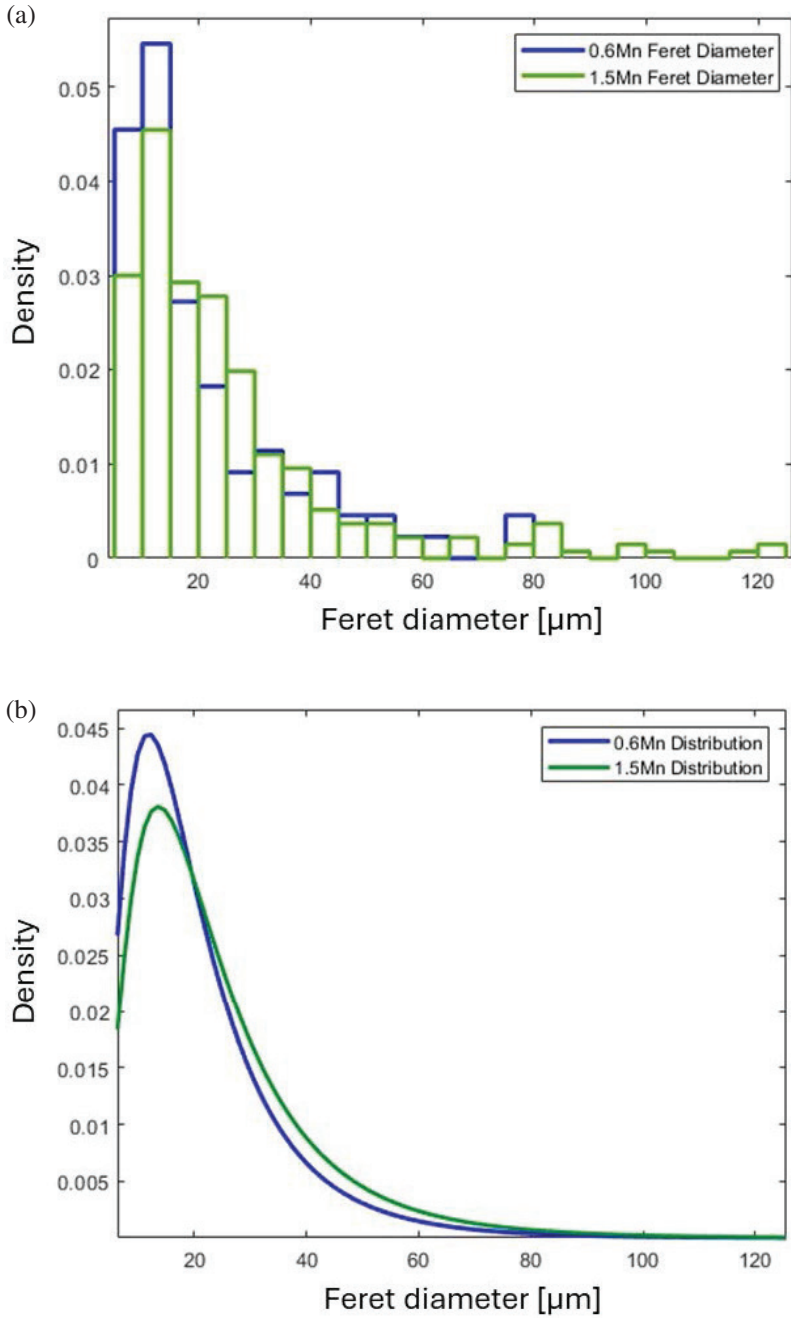


FIGURE 4
 a) A histogram plot of the probability density function (PDF) against the Feret diameter; b) the histogram in a) fitted with a lognormal distribution

distribution and separation efficiency. Also, further research needs to be done on the nucleation and growth kinetics of Fe-bearing intermetallic particles.

The decrease of Fe content at the top part of the melt (Figure 3b) is noticeable. The similar Fe content in the filtered and unfiltered samples (at the top of the melt) suggests that the filter did not remove Fe-bearing intermetallic particles. Also, using the spectrometer, the average Fe contents of the 0.6Mn and 1.5Mn alloys at the bottom of the melt were 0.58 ± 0.05 and 0.67 ± 0.11 wt%, which is significantly higher than the Fe content at the top part of the melt at the lowest temperature. Note that since the spectrometer's analysis points cover a wide area, the average Fe content is the sum of both the Fe-bearing particles and the matrix being measured here. In addition, the amount of the Fe-bearing intermetallic particles at the bottom of the crucible, when compared to the top of the melt sample (Table 3), shows that there are more Fe-bearing intermetallic particles, in both 0.6Mn and 1.5Mn alloys, over the same analysed area. Combining these results, the decreasing Fe content in the top part of the melt is likely due to the sedimentation of the Fe-bearing intermetallic particles at the bottom of the crucible. Therefore, this analysis suggests that the sedimentation of most large Fe-bearing intermetallic particles from the top part of the melt occurs within the experimental time duration. Consequently, the Fe content of the top part of the melt becomes depleted as the Fe-bearing intermetallic particles migrate downwards, leading to a difference in the Fe concentration from the top to the bottom of the melt. This phenomenon is reasonable because the Fe-bearing intermetallic particles have a higher density (around $3.6 \text{ g}\cdot\text{cm}^{-3}$ between 863 to 1023 K [14]) than the liquid Al-Si alloy (2.40 to $2.45 \text{ g}\cdot\text{cm}^{-3}$ within the same temperature range [14]).

The Fe-bearing intermetallic particles were then analysed using SEM in conjunction with EDS to identify and quantify the elemental composition of the Fe-bearing intermetallic particles. A typical EDS spectrum on one of the particles is shown in Figure 5. Figure 5a represents an SEM micrograph of the microstructure; the polygonal particles are primary Fe-based compounds. Figure 5b shows the same micrograph in a) with the Fe-bearing intermetallic particles selected (the green particles). These particles were then analysed for quantitative image analysis and EDS analysis. The green particles were chosen for the analysis, and the turquoise particle (Figure 5c) was selected to show the EDS spectrum related to them.

For the 1.5 Mn and 0.6 Mn additions, a total of 412 and 1660 particles were analysed with the EDS, respectively. The analysis revealed that the average content of Fe in the Fe-bearing intermetallic particles for 0.6 Mn addition was 11.4 ± 0.8 wt%; when 1.5wt% Mn was added, the average Fe content in the particle decreased to around 7.8 ± 0.5 wt%, as summarised in Table 4.

The Fe removal potential using varying amounts of Mn to promote the formation of Fe-bearing intermetallic particles was assessed by combining

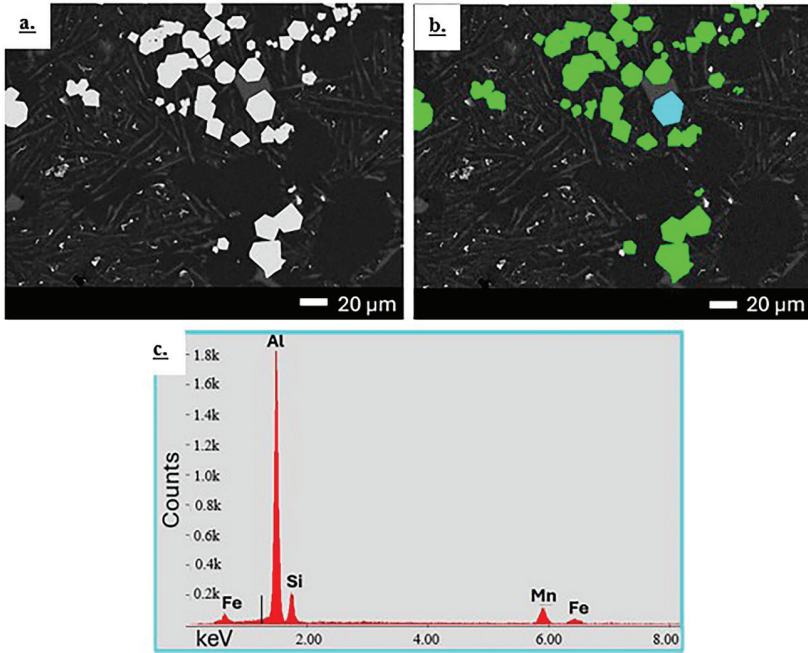


FIGURE 5 a) SEM micrograph; b) the same micrograph in a) with the selected particles; c) EDS spectrum of the turquoise particle.

TABLE 4 Summary of Fe-bearing intermetallic particles results

Alloy	Fe-bearing intermetallic particles area fraction (%)	Total Number of Fe-bearing intermetallic particles	Average Fe content in Fe-bearing intermetallic particles (wt%)	Fe Removal Potential (%)
0.6 Mn	1.9 ± 0.5	88	11.4 ± 0.8	0.22 ± 0.06
1.5 Mn	5.3 ± 0.9	273	7.8 ± 0.5	0.41 ± 0.08

the total amount of Fe contained in the Fe-bearing intermetallic particles and the overall area fraction of the Fe-bearing intermetallic particles (Equation 2):

$$\phi_{Fe} = f_{Fe,p} \times w_{Fe,p} \tag{2}$$

where ϕ_{Fe} is the Fe removal potential (%), $f_{Fe,p}$ is the area fraction of the Fe-bearing intermetallic particles (%) and $w_{Fe,p}$ is the average Fe content in the Fe-bearing intermetallic particles (wt%). The results are summarised in Table 4. The findings indicate that adding 1.5 wt% Mn nearly doubles the Fe removal potential despite the lower Fe content in the Fe-bearing intermetallic

particles. This increased Fe removal potential was attributed to the significantly higher number formed with the 1.5 wt% Mn addition than the 0.6 wt% Mn addition. In conclusion, the decrease of the Fe content in the melt was mainly attributed to the Mn addition increase, as 1.5Mn addition has a higher Fe removal potential than 0.6Mn addition.

4 CONCLUSION

In this paper, the influence of different Mn additions for low Fe composition EN AB-44300 aluminium alloy at a constant cooling rate was investigated. Mn containing Fe-bearing intermetallic former works well for lower Fe compositions in the melt as a Fe-remover agent. However, larger amounts of Mn are required to increase the efficiency of Fe removal in the melt. The presented experiments show the Fe reduction from 0.5 to 0.2 wt%. Specifically, the addition of 1.5 wt% Mn nearly doubled the Fe removal potential despite the lower Fe content in the Fe-bearing intermetallic particles, which was due to the significantly greater number of the Fe-bearing intermetallic particles formed compared to the 0.6 wt% Mn addition. Therefore, the reduction of the Fe content in the melt was primarily attributed to the increased Mn addition, as 1.5Mn addition has a higher Fe removal potential than 0.6Mn addition. The Fe-bearing intermetallic particles sedimented from the top part of the melt within the experimental time duration.

ACKNOWLEDGEMENT

The authors thank Vinnova and the Metallic Materials Programme for financially supporting the project Kliral – Climate-adapted purified aluminium (contract 2022-00819).

REFERENCES

- [1] J. Wu, F. Djavanroodi, C. Gode, S. Attarilar, M. Ebrahimi, Melt refining and purification processes in Al alloys: a comprehensive study, *Mater Res Express* 9 (2022) 032001. <https://doi.org/10.1088/2053-1591/ac5b03>.
- [2] T. Hiraki, T. Miki, K. Nakajima, K. Matsubae, S. Nakamura, T. Nagasaka, Thermodynamic Analysis for the Refining Ability of Salt Flux for Aluminum Recycling, *Materials* 7 (2014) 5543–5553. <https://doi.org/10.3390/ma7085543>.
- [3] D. Raabe, D. Ponge, P.J. Uggowitzer, M. Roscher, M. Paolantonio, C. Liu, H. Antrekowitsch, E. Kozeschnik, D. Seidmann, B. Gault, F. De Geuser, A. Deschamps, C. Hutchinson, C. Liu, Z. Li, P. Prangnell, J. Robson, P. Shanthraj, S. Vakili, C. Sinclair, L. Bourgeois, S. Pogatscher, Making sustainable aluminum by recycling scrap: The science of “dirty” alloys, *Prog Mater Sci* 128 (2022) 100947. <https://doi.org/10.1016/j.pmatsci.2022.100947>.
- [4] B. Wan, W. Li, F. Liu, T. Lu, S. Jin, K. Wang, A. Yi, J. Tian, W. Chen, Determination of fluoride component in the multifunctional refining flux used for recycling aluminum scrap,

- Journal of Materials Research and Technology 9 (2020) 3447–3459. <https://doi.org/10.1016/j.jmrt.2020.01.082>.
- [5] R. Kakitani, A.V. Rodrigues, C. Silva, A. Garcia, N. Cheung, The roles of solidification cooling rate and (Mn,Cr) alloying elements in the modification of β -AlFeSi and hardness evolvments in near-eutectic Al-Si alloys, *Journal of Alloys and Metallurgical Systems 1* (2023) 100005. <https://doi.org/10.1016/j.jalmes.2023.100005>.
- [6] O. Majidi, S.G. Shabestari, M.R. Aboutalebi, Study of fluxing temperature in molten aluminum refining process, *J Mater Process Technol* 182 (2007) 450–455. <https://doi.org/10.1016/j.jmatprotec.2006.09.003>.
- [7] B.G. Dietrich, H. Becker, M. Smolka, A. Keßler, A. Leineweber, G. Wolf, Intermetallic Sludge Formation in Fe Containing Secondary Al-Si Alloys Influenced by Cr and Mn as Preparative Tool for Metal Melt Filtration, *Adv Eng Mater* 19 (2017) 1700161. <https://doi.org/10.1002/adem.201700161>.
- [8] J.M. Sanchez, M. Arribas, H. Galarraga, M. Garcia de Cortazar, M. Ellero, F. Girot, Effects of Mn addition, cooling rate and holding temperature on the modification and purification of iron-rich compounds in AlSi10MnMg(Fe) alloy, *Heliyon* 9 (2023) e13005. <https://doi.org/10.1016/j.heliyon.2023.e13005>.
- [9] S. Hegde, K.N. Prabhu, Modification of eutectic silicon in Al–Si alloys, *J Mater Sci* 43 (2008) 3009–3027. <https://doi.org/10.1007/s10853-008-2505-5>.
- [10] R. Podprocká, D. Bolibruchová, M. Chalupová, Reducing the Negative of the Iron in the Alloy Based on Al-Si-Mg by Manganese, *Archives of Foundry Engineering* 17 (2017) 212–216. <https://doi.org/10.1515/afe-2017-0077>.
- [11] L. Zhang, J. Gao, L.N.W. Damoah, D.G. Robertson, Removal of Iron From Aluminum: A Review, *Mineral Processing and Extractive Metallurgy Review* 33 (2012) 99–157. <https://doi.org/10.1080/08827508.2010.542211>.
- [12] S. Ferraro, A. Fabrizi, G. Timelli, Evolution of sludge particles in secondary die-cast aluminum alloys as function of Fe, Mn and Cr contents, *Mater Chem Phys* 153 (2015) 168–179. <https://doi.org/10.1016/j.matchemphys.2014.12.050>.
- [13] D. SONG, Y. Zhao, Z. Wang, Y. Jia, H. Huang, D. Zhang, W. Zhang, Effect of Mn/Fe ratio on Fe removal efficiency and tensile ductility of an Al–7.0Si–2.4Fe alloy, *J Mater Res* 36 (2021). <https://doi.org/10.1557/s43578-021-00194-6>.
- [14] Thermo-Calc Software TCAL8/Al-alloys Database version 8.2, (n.d.). <https://thermocalc.com/products/databases/aluminum-based-alloys/> (accessed June 27, 2024).